Additive and Subtractive Hybrid Manufacturing (ASHM) of 316L Stainless Steel: Single-Track Specimens, Microstructure, and Mechanical Properties

YUYING YANG,[1] YADONG GONG,[1,2][2] SHUOSHUO QU,[1]
GUOQIANG YIN,[1] CHUNYOU LIANG,[1] and PENGFEI LI[1]

1.—School of Mechanical Engineering and Automation, Northeastern University, Shenyang 110819, China. 2.—e-mail: gongyd@mail.neu.edu.cn

The present work investigates the influence of the laser power (P) and scanning speed (v) on the surface morphology and Vickers microhardness of single scan tracks formed by directed energy deposition (DED) to determine suitable parameter values for further in-depth investigation of additive and subtractive hybrid manufacturing (ASHM) of fabricated parts. The experimental results show that the depth and width of the melt pool depended significantly on both P and v. Furthermore, the anisotropic mechanical behavior of bulk 316L specimens fabricated by ASHM in the horizontal (H), edge (E), and vertical (V) directions relating to the build layers was also explored. The results show that the tensile strength of the specimens fabricated by ASHM in the H direction was higher than that of those built in the E or V direction, implying that the anisotropy originates from the unique thermal history of each component location owing to the layer-by-layer nature of the DED process.

List of Symbols

Abbreviations

DED	Directed energy deposition
ASHM	Additive and subtractive hybrid manufacturing
AM	Additive manufacturing
SM	Subtractive manufacturing
FDM	Fused deposition modelling
SLM	Selective laser melting
316LSS	316L stainless steel
LSCM	Laser scanning confocal microscopy
SEM	Field-emission scanning electron microscopy
WEDM	Wire electrical discharge machining
UTS	Ultimate tensile strength
YS	Yield strength
ETF	Elongation to fracture

Notation

H	Horizontal
E	Edge
V	Vertical
Q_v	Powder feed rate
P	Laser power
v	Scanning speed
h	Layer thickness
t	Hatch spacing
D	Laser beam spot size
f_z	Feed per tooth
V_Z	Milling linear speed
a_p	Amount of axis feed
a_e	Amount of radial feed
Ma	Marangoni convection
ΔT	Temperature gradient
r_m	Radius of the melt pool
α	Thermal diffusivity of the melt pool
T_0	Room temperature
AR	Absorption rate
k	Heat transfer coefficient
d	Penetration depth
T	Operating temperature
T_m	Melting point
ω	Surface tension
μ	Dynamic viscosity of the melt pool
m	Atomic mass
k_b	Boltzmann's constant

INTRODUCTION

Directed energy deposition (DED) is a method for additive manufacturing (AM) of metal components, wherein a continuously directed laser beam delivers

material powder through coaxial nozzles to the melt pool.[1] This technique can be driven by three-dimensional computer-aided design software and relies on layer-by-layer melting to directly manufacture near-full-density final components without using a mold. This process is attracting increasing interest because it enables fabrication of complex-shaped or functionally graded components at low cost in short times for wide used in the automobile, aerospace, and medical fields.[2,3] However, the dimensional accuracy and surface quality cannot meet current industrial demands due to the stair effect, which is intensified by the layer-by-layer accumulation mode and high thermal gradients due to the full melting and solidification that occur in a very short time during the DED process.[4] Since conventional subtractive manufacturing (SM) (such as milling, grinding, and turning) offers high surface quality and dimensional accuracy, it can compensate for the deficiencies of DED.[5,6] However, it is difficult or even impossible to fabricate relatively complex components using SM in isolation. Therefore, additive and subtractive hybrid manufacturing (ASHM) was introduced to inherit the advantages of both AM and SM by using them alternately in one setup. According to relevant literature, in comparison with the single AM process, this technique can significantly improve the surface quality and reduce the production time while minimizing material waste, enabling new applications and opportunities. It thus has significant practical value for application in industrial production.[7,8]

Many researchers have begun to pay close attention to academic investigation of this technology, and some relevant papers have been published.[9–11] Lee et al.[9] used a hybrid rapid prototyping system that combined rapid prototyping by fused deposition modeling (FDM) with a five-axis machining tool to fabricate parts with certain complex characteristics. The system could rotate on a five-axis machine to convert between FDM and CNC machining, thus increasing the stiffness and obtaining more precise dimensions or a better surface finish. Praniewicz et al.[10] employed hybrid manufacturing to repair metal parts, offering an improvement over the adaptive geometry transformation method for the repair region by increasing the material utilization to 42.2% and reducing the machining time by 17.8%. Zhang et al.[11] investigated the influence of the milling thickness on the accuracy of ASHM wire deposition. The results showed that the surface roughness and machining allowance were reduced compared with pure additive manufacturing, due to the change in the melt flow. It is generally known that components fabricated by the DED process have some defects and stress risers, including, among others, unmelted or partially melted powder, hot cracks, voids, and hot stress, because each location suffers from rapid melting and solidification with a unique thermal history.[12,13]

To achieve ASHM components with better surface finish, the additive DED manufacturing method must be tailored. Previous studies have focused primarily on the DED process parameters, with the goals of improving understanding of what occurs during the DED process and reducing the aforementioned defects.[14,15] DED process parameters such as the laser power (P), laser scanning speed (v), layer thickness (d), powder feed rate (Q_v), hatch spacing (t), build direction, and scanning strategy affect the microstructure and corresponding mechanical characteristics of the final metal sample.[16–18] Liverani et al.[16] studied the influence of P, t, and the build direction on the microstructure and mechanical behavior in the selective laser melting (SLM) process. The results showed that density above 98% could be obtained for further study of microstructural and mechanical behaviors. AlMangour et al.[17] described the effect of the feedstock powder preparation method (either direct mixing or ball milling) on the density and mechanical properties of SLM TiB_2/316L SS composites. The results showed that the use of a laser can make the ball-milled powder more homogeneous; moreover, the hardness and wear resistance decreased as the hot isostatic pressing (HIP) holding time was increased. Xiong et al.[18] employed an SLM technique to manufacture supersaturated silver alloy and studied its morphology, density, and mechanical characteristics. The highest relative density obtained was 96.7%, and the highest hardness was 148.9 HV. In reviews and summaries of existing literature, it is noted that process parameters have a marked impact on the microstructure and mechanical characteristics of AM components, due to changes in the melting and solidification processes. The anisotropy of AM-fabricated samples is their main drawback compared with traditional wrought products. Moreover, to obtain fine surface quality, appropriate milling parameters should also be considered.[19,20] Zhu et al.[19] studied the milling stability of thin-walled components using an enhanced multifrequency solution. A relative transfer function was introduced to take into account the dynamic characteristics of the milling tool and workpiece. An enormous amount of research effort has been focused on AM or SM manufacturing processes in terms of the microstructural properties of various materials, such as austenitic stainless steels including 316L stainless steel (hereinafter 316L SS) and 304 stainless steel. However, systematic, comprehensive investigations of HPDM-manufactured parts obtained using different process parameter values to achieve industry-acceptable quality have rarely been reported.

In the work presented herein, 316L SS powder was employed as starting material to fabricate metal components. This 316L SS material is low carbon and easily welded, and has high corrosion resistance due to its Mo, Cr, and Ni contents, being widely applied in aerospace, chemical processing,

Additive and Subtractive Hybrid Manufacturing (ASHM) of 316L Stainless Steel: Single-Track
Specimens, Microstructure, and Mechanical Properties

761

and other fields.[16,17,21] First, we investigated the effect of P and v on the surface topography and Vickers microhardness, respectively, of single-track samples produced using the directed energy deposition (DED) AM technique. The aim of this study is to determine suitable parameter values for further in-depth investigation of their effect on the microstructure and mechanical properties of ASHM-fabricated parts and thereby lay a solid foundation for the technique. Furthermore, the influence of different build directions, viz. horizontal (H), edge (E), and vertical (V), on the mechanical, e.g., tensile, properties of 316L SS parts relating to the build layers was detailed and is systematically discussed. The results of this study may provide a theoretical foundation for ASHM to increase its efficiency, reduce its cost and lead time, and enable reliable fabrication of 316L SS components with optimized mechanical properties.

EXPERIMENTAL PROCEDURES

Powder Material and Experiment

In this work, gas-atomized 316L powder with composition Fe-0.02C-0.5Si-1.2Mn-17Cr-13Ni-2.5Mn (all in mass%) with spherical shape and size range of 10 μm to 120 μm was used as starting material. To prevent oxidization and the entry of humidity, the powder was stored vacuum-packed. The additive and subtractive hybrid manufacturing (ASHM) process of metal parts, which combines additive DED and subtractive milling together in a single entity, is illustrated in Fig. 1a–c. Additive DED uses a layer-by-layer process to deposit molten powder material using a laser beam, being one of most economical and effective methods for depositing molten metallic material. During the ASHM process, the H document of the part's three-dimensional model in the UG design platform is passed to the ASHM software system (SVW80C-3D, Dalian

Hybrid-wise Additive Manufacturing Technology Co., Ltd, China.). Then, the work route and CNC command codes are autogenerated by the software. Next, the additive DED process and five-axis CNC milling are integrated to form a hybrid additive and subtractive machine. Figure 1d and e shows examples of the additive deposition and CNC milling process, respectively.

In this study, alternating additive/subtractive machine operation was applied for the bulk volume; after the deposition of every four layers, a subtractive milling process was carried out to obtain the set height. During the DED process, an alternating x/y-raster scanning method was used; in other words, the scanning direction of each layer was rotated by 90° from the previous layer, with every four layers making up one deposition period, as shown in Fig. 2a. The other controllable parameters are P and v. The ASHM process parameters are presented in detail in Table I. A 40 steel with dimensions of 160 mm × 160 mm × 20 mm was used as the substrate; before laser scanning, the surface of the substrate was milled successively to eliminate the very thin oxide layer. To determine the optimal additive DED parameter values, single tracks with length of 40 mm were fabricated by DED in the ASHM process for characterization and to investigate the influence of P and v on the surface topography, melt pool dimensions, and Vickers hardness development. Single-track specimens were thus produced at constant P = 1000 W with various v values from 280 mm/min to 600 mm/min, and at constant v = 360 mm/min but with different P values ranging from 800 W to 1200 W. Finally, the effects of the build direction on the tensile behavior and attendant fracture morphology were studied. Samples were also manufactured by ASHM using three different orthogonal build directions, viz. horizontal (H), edge (E), and vertical (V); a schematic showing the dimensions for mechanical
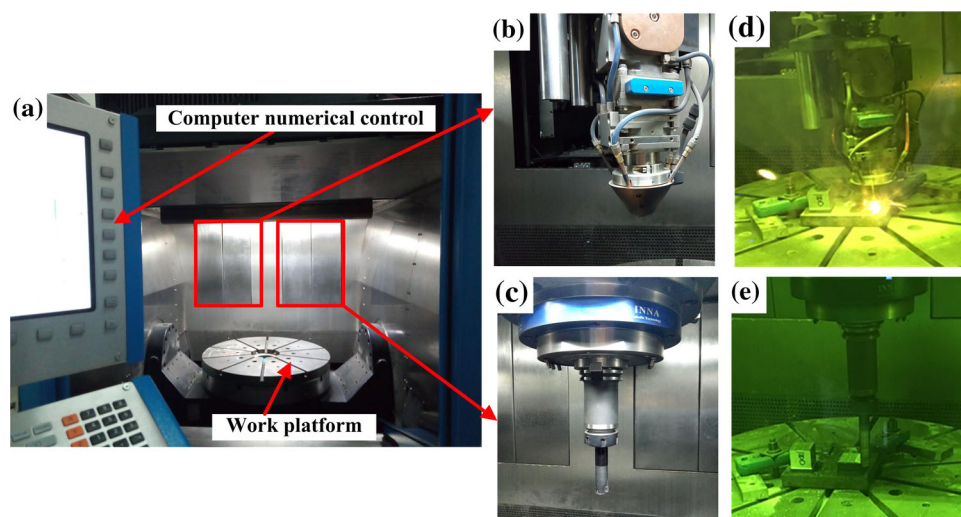

Fig. 1. ASHM experiment equipment: (a) ASHM experiment; (b) additive laser head; (c) subtractive milling head, (d) example of additive deposition process; (e) example of CNC milling.
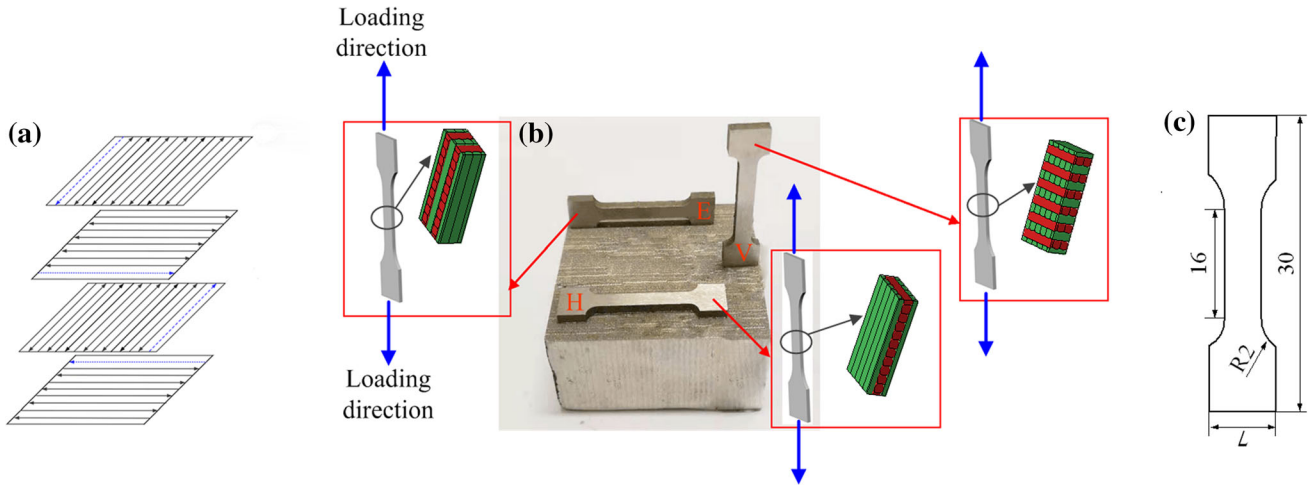
Fig. 2. ASHM-fabricated 316L SS cubic component: (a) schematic diagram of DED process scanning strategies in the ASHM process; (b) different types of tensile samples in three directions: H, E, and V; (c) schematic showing the dimensions for mechanical testing.

Table I. Material properties and ASHM process parameter conditions

	Unit	Values
Laser power, P	W	600, 800, 1000, 1200,
Scanning speed, v	mm/min	240, 360, 440, 520, 600
Laser beam spot size, D	mm	3
Powder feed rate, Qv	g/min	1
Layer thickness, h	mm	0.5
Focal length	mm	13.5
Hatching distance, t	mm	1
Feed per tooth, f_z	mm	0.25
Milling linear speed, V_Z	m/min	120
Amount of axis feed, a_p	mm	0.5
Amount of radial feed, a_e	mm	0.2

testing according to ISO 6892-1[17] is presented in Fig. 2b and c.

Characterization

The morphology of single-line scanning track specimens was first characterized by laser scanning confocal microscopy (LSCM). A cross-section of the single-track specimen was prepared for microstructure analysis using standard metallographic methods (grinding and polishing). A solution of 8 g $CuSO_4$ and 40 ml HCl in 40 ml distilled water was used as the etchant for the polished specimens. The microstructure of the single-line scanning track samples after etching was observed by LSCM.

The Vickers microhardness of single-track specimens in the melt pool during the ASHM DED process was measured using a 430SVD Vickers microhardness testing machine (Wilson Hardness, USA) on the polished surface with a load of 1000 gF and loading duration of 10 s. To investigate the scanning speed over the width and depth of a single-track sample, the Vickers hardness was obtained at different positions along the vertical and horizontal directions.

Tensile testing samples were sectioned from the ASHM-fabricated 316L SS cubic part by wire electrical discharge machining (WEDM) in the H, E, and V build directions. The room-temperature tensile characteristics, viz. ultimate tensile strength (UTS), yield strength (YS), and elongation to fracture (ETF), were measured using a WDW-100E electronic universal material testing machine at a strain rate of 0.001 s^{-1}. According to ISO 6892-1, the strain rate should not exceed 0.0025 s^{-1} within the plastic range and up to the specified strength (specified plastic extension strength, specified total extension strength, and specified residual extension strength). Further details on this testing method also can be found in Refs. 17, 22, and 23. At least three test samples were tested for each build direction. Finally, the morphology of the tensile fracture surfaces was investigated by super depth field-emission scanning electron microscopy (SEM).

RESULTS AND DISCUSSION

Analysis of a Single Melting Track

The ability to manufacture uniform, high-quality single tracks is one of the important factors affecting the achievement of high quality and geometric accuracy.[24] Single tracks with length of 40 mm were manufactured by DED as part of ASHM. After construction, the single tracks were cut perpendicular to the laser scanning direction to study and analyze the specimen morphology in the vertical (V) and horizontal (H) directions. Figure 3 shows the surface topography on single scan tracks obtained using the five different v values of 280 mm/min, 360 mm/min, 440 mm/min, 520 mm/min, and 600 mm/min with constant $P = 1000$ W in the DED control program that manipulates the laser scanning pattern. Figures 3 and 4 show that v and P had different effects on the size and shape of various DED processing parameters, as well as a marked impact on the surface stability of a single scanning path. The flows of the liquid phase in the melt pool are rather complex, with many elements that could lead to mass transfer. Among these effects, Marangoni convection is one of the most critical, affecting the continuity and stability of the scan trace.[25]

When the powder is irradiated by a laser beam, the material absorbs laser energy and then begins to melt when the temperature exceeds the melting point of 316L SS. The temperature gradient in the melt pool leads to a surface tension gradient and is related to the Marangoni convection. The intensity of the Marangoni convection (Ma), a dimensionless measure of the thermally driven surface tension forces versus the viscous forces, can be expressed as[26]

$$\mathrm{Ma} = \frac{\partial \gamma}{\partial T} \frac{r_\mathrm{m}^2 \Delta T}{\mu \alpha},$$

$$(1)$$

where $\frac{\partial \gamma}{\partial T}$ represents the sensitivity of the surface tension of the molten metal to temperature (i.e., the temperature coefficient of the surface tension), while ΔT, r_m, μ, and α represent the temperature gradient, and the radius, dynamic viscosity, and thermal diffusivity of the melt pool, respectively. A higher scanning speed implies a shorter interaction duration between the laser beam and material, which will lead to a reduction of the energy absorption capacity by the material and cause a reduction in the peak temperature of the melt pool. Therefore, ΔT and $\frac{\partial \gamma}{\partial T}$ decreased from the edge to center of the melt pool, thereby moderating the Marangoni flow and the resulting turbulence in the melt pool. In contrast, disturbance in the melt pool will lead to instability between the solid and liquid surface, resulting in a scan track with an unstable surface for the lower values of v. In addition, the material will overheat due to the extraordinarily high temperature resulting at low v, causing evaporation of the metallic material and thus mass loss.[23] Figure 3a shows that, at relatively low scanning speeds of $v \leq 280$ mm/min and $P = 1000$ W, the dwell time of the laser beam on the powder increases, which increases the temperature of the melt pool; moreover, a large amount of powder enters the melt pool and the excessive energy reduces the surface quality of the scan track. Instead, the laser energy will be absorbed by the material at higher scanning speeds. When the scanning speed exceeds a threshold, it is difficult for the laser energy to melt the metal powder completely, thereby resulting in the balling phenomenon. At the same time, the spidery melt pool becomes destabilized and will divide into fragments to obtain a new state of balance. As
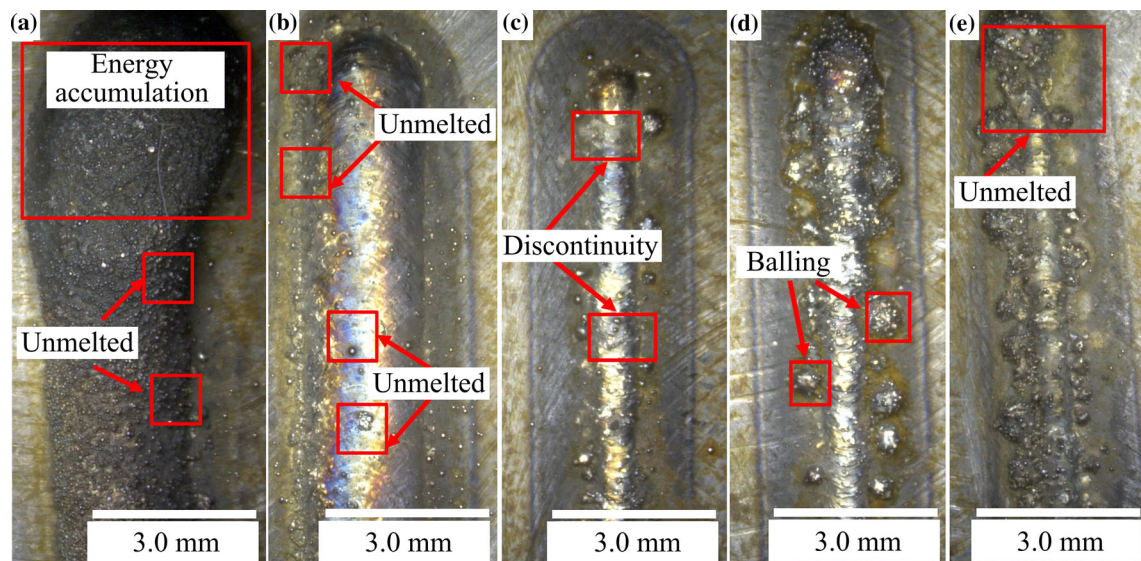

Fig. 3. Surface morphology of 316L specimens fabricated by DED using various values of v: (a) 280 mm/min, (b) 360 mm/min, (c) 440 mm/min, (d) 520 mm/min, and (e) 600 mm/min, with constant $P = 1000$ W.
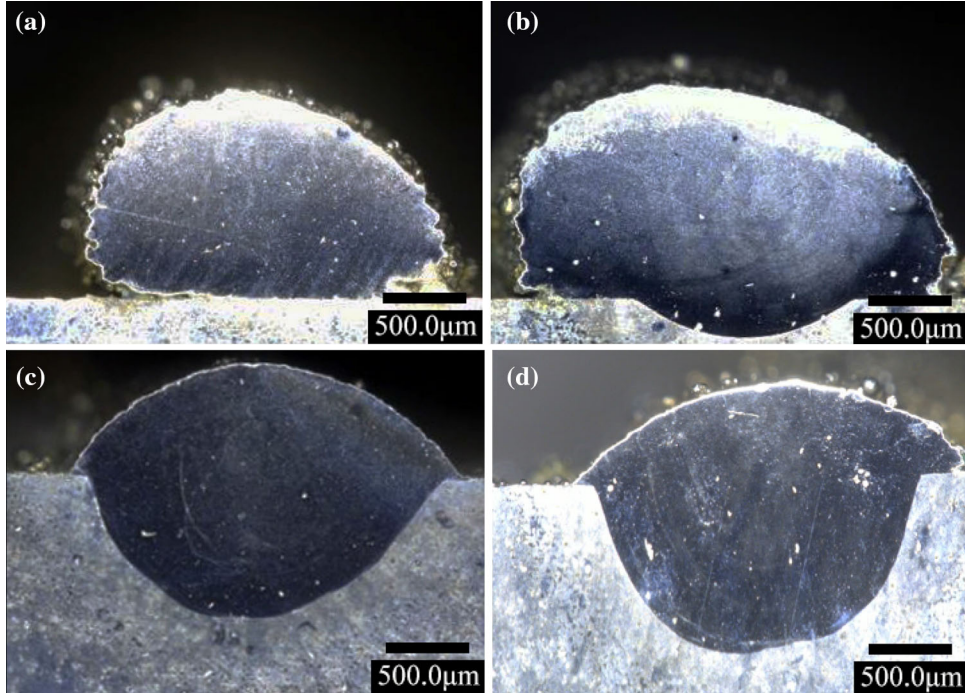
Fig. 4. The cross-sectional morphology of single-scan tracks obtained using various P values of (a) 600 W, (b) 800 W, (c) 1000 W, and (d) 1200 W, with constant v = 360 mm/min.

shown in Fig. 3c–e, at scanning speeds $v \geq 440$ mm/min, the scan trace presented a remarkably unstable surface, including large amounts of unmelted powder particles, discontinuities, and the balling effect. These characteristics are due to the short dwell time of the laser spot (low energy input) and the low penetration of the laser into the powder layer, resulting in a relatively small and low-temperature melt pool. In turn, such features will lead to insufficient melting of the powder and melt flow discontinuity, thus reducing the contact area between the melt pool, metal powder, and substrate. Figure 3b shows that v = 360 mm/min can be considered to be the optimum technical parameter value to form a scan trace with a stable surface, although some unmelted powder remained, which is a common feature of the AM process.

The characteristic microstructures of the cross-section of single scan tracks obtained at different P values ranging from 600 to 1200 W with constant v = 360 mm/min are shown in Fig. 4. The melt pools induced by the interaction between the laser and the material were visible. The curved contour of the melt pool occurred as a result of the intersection of the laser scanning traces and the substrate. Layer-wise microscopic structural nature of the fabricated components was commonly observed, along with a clear semicircular outline of the melt pool, as shown in Fig. 4, which can be attributed to the Gaussian profile of the laser beam. Most of the energy was concentrated at the center of the laser beam, causing deep melting at the center but shallow

melting at the edge of the melt pool. However, the shape, liquid diffusion characteristics, and molten depth and width varied with the P value.

The temperature field of the laser-molten pool was calculated using Eq. (2)[27]:

$$T(z,t) = T_0 + \left[\frac{AR \cdot P/V}{2\pi k \left[t + \left(t + \left(D^2/16\alpha \right) \right) \right]^{1/2}} \right]$$
$$\cdot \exp - \left(\frac{(d + d_0)^2}{4\alpha t} \right) \qquad (2)$$

where T_0 is the room temperature, AR is the absorption rate, k is the heat transfer coefficient, D, t, and d represent the laser beam size, time, and penetration depth, respectively, and α is the thermal diffusivity.

The relationship between the surface tension ω and temperature can be written as Eq. (3)[28]:

$$\omega = [868 - 0.152(T - T_m)] \times 10^{-3}, \quad T > 873, \quad (3)$$

where T and T_m are the operating temperature and melting point, respectively. When $T > T_m$, the powder melts, and ω increases with a decrease in T.

The viscosity μ, which is strongly dependent on T, which was measured using an FLIR A655sc infrared thermometer, can be calculated by Eq. (4)[29]:

$$\mu = \frac{16}{15} \sqrt{\frac{m}{k_b T}} \cdot \omega \qquad (4)$$

where m, k_b, and ω are the atomic mass, Boltzmann constant, and surface tension of the steel matrix, respectively. Equations (2)–(4) indicate that the viscosity of the liquid decreases with a relatively high P.[21]

As shown in Fig. 4, when P increases, T increases while the corresponding ω and μ decrease, indicating much better melting characteristics. For low $P \leq 800$ W, the bonding between the as-fabricated molten trace and substrate is poor, indicating a very short laser penetration depth into the substrate, as shown in Figs. 4a and b. As shown in Fig. 4d, when P reached 1200 W, the depth of the melt pool increased. This occurs because P is too large, thus the amount of meltable powder exceeds the amount of powder actually delivered. The amount of powder entering the melt pool will no longer increase, resulting in the downward tendency of the powder utilization ratio. According to Eqs. (2)–(4), as energy continues to accumulate in the melt pool, T rises, thereby resulting in lower ω and μ, so that the height decreases while the width and depth of the melt pool increase. In fact, the thickness of the single layer will decrease, which will cause the melt pool to be highly deformed, seriously affecting the manufacturing accuracy. Consequently, the surface tension and viscosity characteristics of the melt pool must be carefully controlled to achieve the desired structure in the DED process as part of ASHM.

On the basis of Eq. (2), with an increase of the applied v or a reduction of P, the temperature field in the laser-molten pool will decrease, which leads to the decrease in the depth and width of the melt pool. During the DED process as part of ASHM, the size of the melt pool is on the order of millimeters, or up to centimeters in the lateral direction. Moreover, the penetration depth of the melt pool is much smaller than the width of the melt pool, as shown in Fig. 5a. The width and depth decrease with increasing v. For a P value of 1000 W, the width and penetration depth decreased from 2500 μm and 1600 μm to 1600 μm and 800 μm as the applied v was increased from 280 mm/min to 600 mm/min, respectively. This shallow penetration depth indicates that the particles were partially melted in the DED process, suggesting a risk of increasing the degree of porosity of the DED-fabricated specimens, thus decreasing the densification rate.

During the DED process, the Vickers hardness is related to the content of Mn and Cr. Indeed, the surface hardness value is proportional to the Mn and Cr content. At higher temperatures, material evaporation can cause a loss of volatile elements, particularly Mn and Cr, during the DED process. Such decreases in the content of Mn and Cr during the DED process may thus decrease the hardness of as-built 316L specimens. The Vickers hardness gradually decreased from the top to the bottom of the melt pool (from 316 HV to 275 HV) in the vertical direction, as shown in Fig. 5b. To further evidence this, the elemental content of samples extracted from the edge and center regions of the melt pool in the horizontal direction were studied by energy-dispersive spectroscopy (EDS). The results revealed that the content of Mn and Cr decreased from 7.73% to 4.87% and from 20.18% to 14.09%, respectively, thus the Vickers hardness tended to drop off from the edge to the center of the melt pool (from 330 HV to 280 HV) in the horizontal direction (Fig. 5c). This finding suggests that the rate of Mn and Cr loss from the melt pool increased with increasing temperature. Moreover, the DED-fabricated specimens exhibited higher hardness compared with the 40# steel substrate (point #20) produced by casting (Vickers hardness of 213 HV). Based on the results of this investigation into the effect of P and v on the surface topography and Vickers microhardness, respectively, of single-track samples produced by using DED, suitable parameter values are 1000 W for P and 360 mm/min for v. These results provide theoretical and data support to choose the process parameter values for future work on ASHM.

Effect of Build Direction on Tensile Behavior

Generally, the mechanical behavior of 316L SS manufactured in a layer-by-layer fashion shows a large degree of anisotropy; the build direction greatly influences the mechanical behavior of the manufactured specimens. The engineering tensile stress–strain curves of 316L SS parts manufactured by HASM with different build directions of horizontal (H), edge (E), and vertical (V) at room temperature are presented in Fig. 6a, revealing the effect of the build layers. The results for the YS, UTS, and ETF with error bars are presented and compared with those of cast materials[22] in Fig. 6b. The samples built in the H direction showed not only excellent tensile strength (both UTS and 0.2% YS) of 429.03 MPa and 649.75 MPa, respectively, but also the maximum ETF, when compared with the specimens obtained in the E or V build direction. Moreover, the sample with the V build direction (in which the loading direction is parallel to the build direction; see Fig. 2b) showed the lowest YS, UTS, and ETF values of 381.18 MPa, 596.01 MPa, and 33.13%, respectively. Meanwhile, the part obtained in the E direction showed intermediate YS, UTS, and ETF values of 421.32 MPa, 621.08 MPa, and 33.56%, respectively. This finding can mainly be attributed to the pronounced anisotropy in the tensile properties. When the 316L SS parts were extracted from the specimens built in the H direction, the tensile loading direction was parallel to the layer-by-layer scanning direction (with at least one layer parallel to the scanning direction; see Fig. 2b) and the scanning tracks played a reinforcing role in the bulk sample. However, the parts built in the V direction exhibited much lower ETF values than those built in the H or E direction, firstly because the tensile loading orientation was perpendicular to
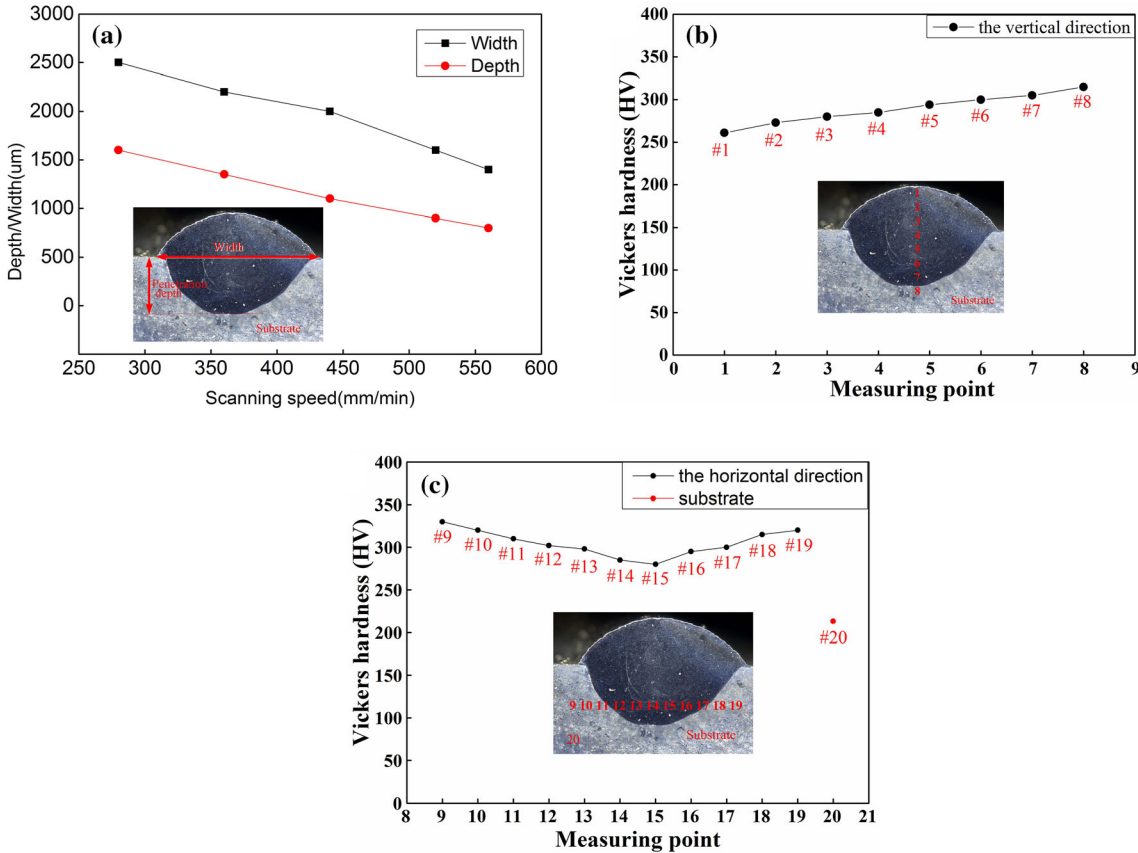
Fig. 5. (a) Effect of *v* on width and depth of melt pool; effect of build direction on Vickers hardness of melt pool in (b) vertical and (c) horizontal direction.
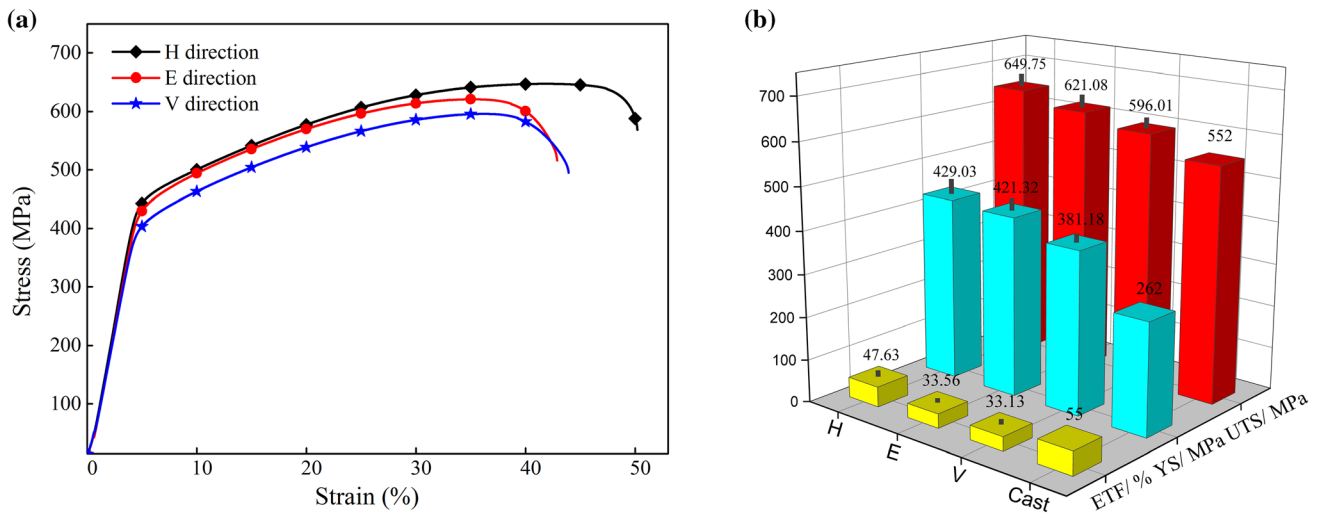

Fig. 6. (a) Stress–strain curves of 316L SS specimens manufactured by HASM with different build directions at room temperature; (b) corresponding mechanical data and comparison with cast materials.

the laser scanning direction (Fig. 2b), and secondly because some localized defects such as pores in sensitive regions, for example, interfaces between layers, led to weak metallurgical bonding between layers. In the E direction, the tensile loading direction was parallel to the building direction

(Fig. 2b), but the sample contained more layers than those built in the H direction, thereby showing slightly lower strength. The YS and UTS values of the HASM-manufactured 316L specimens were much higher those of the cast specimen,[22] while the ETF was much lower (Fig. 6b). This is due to the

Additive and Subtractive Hybrid Manufacturing (ASHM) of 316L Stainless Steel: Single-Track
Specimens, Microstructure, and Mechanical Properties

767

rapid heating and cooling that occur during the DED process, which is beneficial to generate a fine microstructure with high dislocation density, leading to the improvement in the YS and UTS, although the inevitable metallurgical defects (e.g., pores) in the ASHM-fabricated samples decreased their ductility.

To further illuminate the tensile failure mechanism, the fracture surfaces of the tensile samples fabricated by HASM in the H, E, and V directions were studied (Fig. 7). From the lower-magnification SEM micrographs, the sample built in the H direction (Fig. 7a) showed a greater reduction in area compared with those built in the E (Fig. 7c) or V directions (Fig. 7e). Building in the V direction resulted in a lower reduction in area compared with the H and E directions, with the sample built in the

E-direction falling between the other two, which indicates that the sample built in the H direction exhibited the best ductility. The high-magnification SEM micrographs of the fracture surfaces of the samples obtained under the same processing parameters reveal that the specimens manufactured by HASM along the different build directions (H, E, and V) all exhibited almost evenly distributed dimples on the fracture surface, indicating a fairly ductile fracture characteristic (Figs. 7b, d, and f, respectively). On the fracture surface of the sample built along the V direction, a large and noticeable amount of second-phase particles was present. The previous layer will undergo multiple thermal cycles, resulting in precipitation of such second-phase particles during the DED process. They are usually present near dimples, which are also the initial
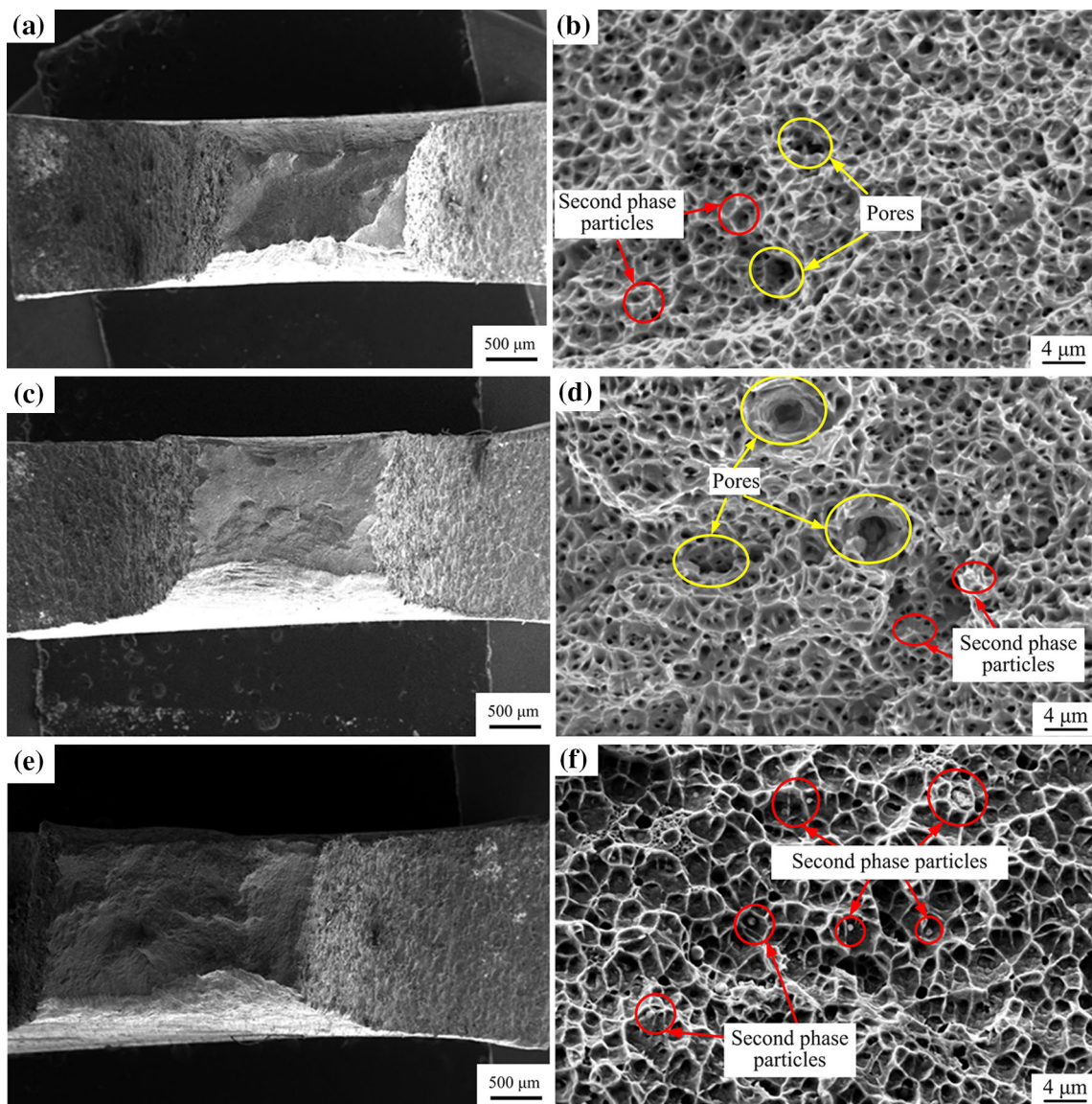

Fig. 7. SEM images showing the fracture surfaces of tensile-tested specimens built in different directions: (a) low magnification, H direction; (b) high magnification, H direction; (c) low magnification, E direction; (d) high magnification, E direction; (e) low magnification, V direction; (f) high magnification, V direction.

positions for crack formation. When tensile loading is applied, microcracks will form due to these larger second-phase particles. This effect will aggravate the fracture during tensile testing, leading to serious degradation in both the tensile strength (UTS and YS) and ductility. According to the layer-based nature of the samples, some defects (e.g., small pores) in sensitive zones such as the interface between subsequent layers would collapse. As shown in Fig. 2, a series of thin-walled samples with dimensions of $30 \times 7 \times 2$ mm^3, $30 \times 2 \times 7$ mm^3, and $7 \times 2 \times 30$ mm^3 were manufactured using the three different build directions of H, E, and V, respectively. The layer thickness was 0.5 mm (Table I). According to the size of the tensile sample, every 4, 14, and 60 layers could be obtain for the H, E, and V direction, respectively. Compared with the H and E direction, the greater number of layers and longer time interval between two successive layers in the sample built in the V direction may be the reasons for its lower degree of strength, as these effects will increase the possibility of inhomogeneous heat transfer and the provision of insufficient heat to remelt the powder particles in the previous layer.[30,31] The sample built in the E direction contained some pores, which could lead to local stress concentrations and crack propagation, thereby reducing the UTS and YS. However, the sample built in the H direction was found not to exhibit significant pores, instead showing relatively elongated and squeezed pores as well as a homogeneous distribution of dimples on the fracture surface. Therefore, the tensile strength and ductility of the sample built in the H direction were the best in comparison with the samples built in the other directions.

CONCLUSION

The effects of P and v on the surface topography of the scanning track of a single-track specimen manufactured using DED as part of additive and subtractive hybrid manufacturing (ASHM) were investigated. The effects of the build direction, viz. horizontal (H), edge (E), and vertical (V), on the mechanical characteristics of AISI 316L SS specimens produced using ASHM were investigated. The results of this study lead to the following main conclusions and findings:

1. For single-track specimens, as v is increased or P is decreased, the depth and width of the melt pool decrease, because the temperature field in the laser melt pool decreases.
2. The Vickers hardness showed a decreasing trend from the top to the bottom of the melt pool (from 316 HV to 275 HV) in the vertical direction. Moreover, the Vickers hardness showed a decreasing trend from the edge to the center of the melt pool (from 330 HV to 280 HV) in the horizontal direction.

3. Compared with the ASHM-fabricated 316L SS specimens built in the E and V directions, the tensile characteristics (UTS, YS, and ETF) of the specimens built in the H direction were noticeably higher, because the loading direction was parallel to the layer-by layer direction. Moreover, the highest mechanical properties were obtained in the H direction, namely UTS of 429.03 MPa, YS of 649.75 MPa, and ETF of 47.63%, indicating the best ductility among the tested samples.
4. Examination of the fracture surface of the sample built in the H direction did not reveal significant crater-like voids, but instead relatively elongated and squeezed pores as well as a homogeneous distribution of dimples. This result implies an improvement in the tensile characteristics of the ASHM-fabricated 316L SS specimens with fewer defects.

REFERENCES

1. F. Weng, S.M. Gao, J.C. Jiang, J.J. Wang, and P. Guo, *Addit. Manuf.* 27, 474 (2019).
2. W. Woo, D.K. Kim, E.J. Kingston, V. Luzin, F. Salvemini, and M.R. Hill, *Mater. Sci. Eng. A Struct.* 744, 618 (2019).
3. B.C. Salzbrenner, J.M. Rodelas, J.D. Madison, B.H. Jared, L.P. Swiler, Y.L. Shen, and B.L. Boyce, *J. Mater. Process. Technol.* 241, 1 (2017).
4. T. Mukherjee, V. Manvatkar, A. De, and T. DebRoy, *Scr. Mater.* 127, 79 (2017).
5. J.H. Yi, J.W. Kang, T.J. Wang, X. Wang, Y.Y. Hu, T. Feng, Y.L. Feng, and P.Y. Wu, *J. Alloys Compd.* 786, 481 (2019).
6. L. Zhu, C. Ni, Z. Yang, and C. Liu, *Precis. Eng.* 57, 229 (2019).
7. S.S. Qu, Y.D. Gong, Y.Y. Yang, X.L. Wen, and G.Q. Yin, *Ceram. Int.* 45, 3059 (2019).
8. P.C. Priarone and G. Ingarao, *J. Clean. Prod.* 144, 57 (2017).
9. J.K. Watson and K.M.B. Taminger, *J. Clean. Prod.* 176, 1316 (2018).
10. W.C. Lee, C.C. Wei, and S.C. Chung, *J. Mater. Process. Technol.* 214, 2366 (2014).
11. M. Praniewicz, T. Kurfess, and C. Saldana, *J. Manuf. Sci. E-T ASME* 141, 1 (2019).
12. S. Zhang, Y.Z. Zhang, M. Gao, F.D. Wang, Q. Li, and X.Y. Zeng, *Sci. Technol. Weld. JOI* 24, 375 (2019).
13. T. Mishurova, S. Cabeza, K. Artzt, J. Haubrich, M. Klaus, C. Genzel, G. Requena, and G. Bruno, *Materials* 27, 4 (2017).
14. P. Mercelis and J.P. Kruth, *Rapid Prototyp. J.* 15, 5 (2006).
15. S.M. Yusuf, Y.F. Chen, R.P. Boardman, and S.F. Yang, *Metals* 7, 64 (2017).
16. D.D. Gu, W. Meiners, K. Wissenbach, and R. Poprawe, *Int. Mater. Rev.* 57, 133 (2012).
17. E. Liverani, S. Toschi, L. Ceschini, and A. Fortunato, *J. Mater. Process. Technol.* 249, 255 (2017).
18. B. AlMangour, D. Grzesiak, and J.M. Yang, *Powder Technol.* 319, 37 (2017).
19. W. Xiong, L. Hao, Y. Li, D.N. Tang, Q. Cui, Z.Y. Feng, and C.Z. Yan, *Mater. Des.* 170, 1 (2019).
20. B.L. Yan and L.D. Zhu, *Int. J. Adv. Manuf. Technol.* 102, 431 (2019).

21. X.H. Lu, Z.Y. Jia, X.X. Wang, Y.B. Liu, M.Y. Liu, Y.X. Feng, and S.Y. Liang, *Measurement* 145, 254 (2019).
22. Y.Y. Yang, Y.D. Gong, S.S. Qu, Y.L. Rong, Y. Sun, and M. Cai, *Int. J. Adv. Manuf. Technol.* 97, 2687 (2018).
23. A. Yadollahi, N. Shamsaei, S.M. Thompson, and D.W. Seely, *Mater. Sci. Eng. A Struct.* 644, 171 (2015).
24. C.L. Qiu, N.J.E. Adkins, and M.M. Attallah, *Acta Mater.* 103, 382 (2016).
25. I. Yadroitsev, P. Krakhmalev, and I. Yadroitsava, *Addit. Manuf.* 7, 45 (2015).
26. I. Yadroitsev, A. Gusarov, I. Yadroitsava, and I. Smurov, *J. Mater. Process. Technol.* 210, 1624 (2010).
27. D.H. Dai and D.D. Gu, *Appl. Surf. Sci.* 355, 310 (2015).
28. P. Wei, Z.Y. Wei, Z. Chen, J. Du, Y.Y. He, J.F. Li, and Y.T. Zhou, *Appl. Surf. Sci.* 408, 38 (2017).
29. J.Y. Zhang, D.D. Gu, Y. Yang, H.M. Zhang, H.Y. Chen, D.H. Dai, and K.J. Lin, *Engineering* 5, 736 (2019).
30. I. AlMangour, D. Grzesiak, T. Borkar, and J.M. Yang, *Mater. Des.* 138, 119 (2018).
31. Z.Q. Wang, T.A. Palmer, and A.M. Beese, *Acta Mater.* 110, 226 (2016).